LETTER

Visible–frequency hyperbolic metasurface

Alexander A. High[1,2]*, Robert C. Devlin[3]*, Alan Dibos[3], Mark Polking[1], Dominik S. Wild[2], Janos Perczel[2,4], Nathalie P. de Leon[1,2], Mikhail D. Lukin[2] & Hongkun Park[1,2]

Metamaterials are artificial optical media composed of sub-wavelength metallic and dielectric building blocks that feature optical phenomena not present in naturally occurring materials[1–7]. Although they can serve as the basis for unique optical devices that mould the flow of light in unconventional ways, three-dimensional metamaterials suffer from extreme propagation losses[8,9]. Two-dimensional metamaterials (metasurfaces) such as hyperbolic metasurfaces for propagating surface plasmon polaritons[10,11] have the potential to alleviate this problem. Because the surface plasmon polaritons are guided at a metal–dielectric interface (rather than passing through metallic components), these hyperbolic metasurfaces have been predicted to suffer much lower propagation loss while still exhibiting optical phenomena akin to those in three-dimensional metamaterials. Moreover, because of their planar nature, these devices enable the construction of integrated metamaterial circuits as well as easy coupling with other optoelectronic elements. Here we report the experimental realization of a visible-frequency hyperbolic metasurface using single-crystal silver nanostructures defined by lithographic and etching techniques. The resulting devices display the characteristic properties of metamaterials, such as negative refraction[1–5] and diffraction-free propagation[6,7], with device performance greatly exceeding those of previous demonstrations. Moreover, hyperbolic metasurfaces exhibit strong, dispersion-dependent spin–orbit coupling, enabling polarization- and wavelength-dependent routeing of surface plasmon polaritons and two-dimensional chiral optical components[12–15]. These results open the door to realizing integrated optical metacircuits, with wide-ranging applications in areas from imaging and sensing to quantum optics and quantum information science.

Our approach for realizing a visible-frequency hyperbolic metasurface (HMS) involves the definition of a nanometre-scale silver/air grating on a sputter-deposited, single-crystalline silver film by electron-beam lithography and plasma etching. Unlike focused-ion-beam milling methods[5,12], which produce rough, defect-ridden structures, this new method produces smooth, high-quality silver nanostructures with high aspect ratios, critical for the realization of a surface plasmon polariton (SPP)-HMS. Figure 1 illustrates the materials and structures that form the basis for HMSs. As a starting material, we sputter-deposited a micrometre-thick silver film on a (111)-silicon substrate at 300°C and at high deposition rate (>1.5 nm s^{-1})[16,17]. High-resolution transmission electron microscopy (Fig. 1a), X-ray diffraction, atomic force microscopy, and electron backscatter diffraction measurements (see Supplementary Figs 1, 2 and 3, respectively) reveal that these films are single-crystalline and have root-mean-square roughnesses as low as 300 pm. The ellipsometric characterization (Supplementary Fig. 4) shows that, over a large portion of the visible spectrum, the optical loss in our film is much lower than those reported previously[18,19] and is comparable to recently reported silver films prepared by molecular beam epitaxy[20]. Unlike the molecular beam epitaxy process[20], however, the sputtering process can rapidly grow single-crystalline films of large thicknesses,

which is crucial for the realization of an HMS because it prevents SPP absorption by the silicon substrate. From the experimentally measured dielectric constants, we determine that the SPP propagation length L_p (defined as the length over which the SPP intensity decays by $1/e$) in a silver film exceeds 100 μm for far-field wavelengths $λ$ greater than 650 nm (Fig. 1b).

Beyond exceptional optical performance, single-crystalline silver films offer mechanical and thermodynamic stability, which is crucial for defining nanoscale features using lithography and etching. We fabricated the silver/air gratings and light in- and out-coupling structures (used to convert far-field light into SPPs and vice versa) by first defining an Al$_2$O$_3$ hard mask with electron-beam lithography and then dry-etching silver with argon plasma (see Supplementary Fig. 6 for details). After etching, the residual Al$_2$O$_3$ mask was removed with hydrofluoric acid, leaving clean, high-aspect-ratio silver features. Figure 1d and e show scanning electron microscope (SEM) images of representative devices (schematically shown in Fig. 1c with silver ridge height $h = 80$ nm, width $w = 90$ nm, and pitch $a = 150$ nm). The smooth surface of our devices, coupled with the single-crystalline nature of silver, minimizes extrinsic optical losses originating from grain boundaries and surface roughness.

A recent theoretical work[11] has predicted that a silver/air grating with appropriate sub-wavelength feature sizes, such as that shown in Fig. 1d and e, should exhibit hyperbolic dispersion for propagating SPPs below a critical wavelength, $λ = λ_T$ (and elliptical dispersion above it). A simple physical picture provides insight into the transition from hyperbolic to elliptical dispersion in this structure. At short wavelengths, the plasmonic modes are tightly confined to the ridges of the grating, qualitatively similar to the situation in an array of parallel nanowires that exhibits hyperbolic dispersion[21]. In the long wavelength limit, on the other hand, the modes are only weakly confined, and the grating can be considered a perturbation to a flat surface, resulting in elliptical dispersion (for discussion, see Supplementary Figs 7 and 8).

To experimentally verify these predictions, we fabricated a series of devices and tested their optical properties. Figure 2 presents a device, D1, designed to demonstrate negative refraction of SPPs, a known property of hyperbolic metamaterials[22]. This device consists of a silver/air grating as well as a groove that launches SPPs on flat silver upon far-field excitation (Fig. 2a). The angle of refraction at the flat silver/grating interface was determined by collecting scattered light at the in-coupling structure, the silver-film/grating interface, and the corresponding out-coupling structure. As is clearly shown in Fig. 2b and d (see also Supplementary Figs 9 and 10), the behaviour of D1 changes from normal refraction at $λ > 540$ nm to negative refraction at $λ < 540$ nm. We note that $λ_T$, at which the device behaviour changes from normal to negative refraction (that is, elliptical to hyperbolic dispersion), can be tuned by varying the device geometry (Supplementary Fig. 11a) or by changing the dielectric environment of silver (for example, by depositing a thin layer of Al$_2$O$_3$ on the device; see Supplementary Fig. 11b).
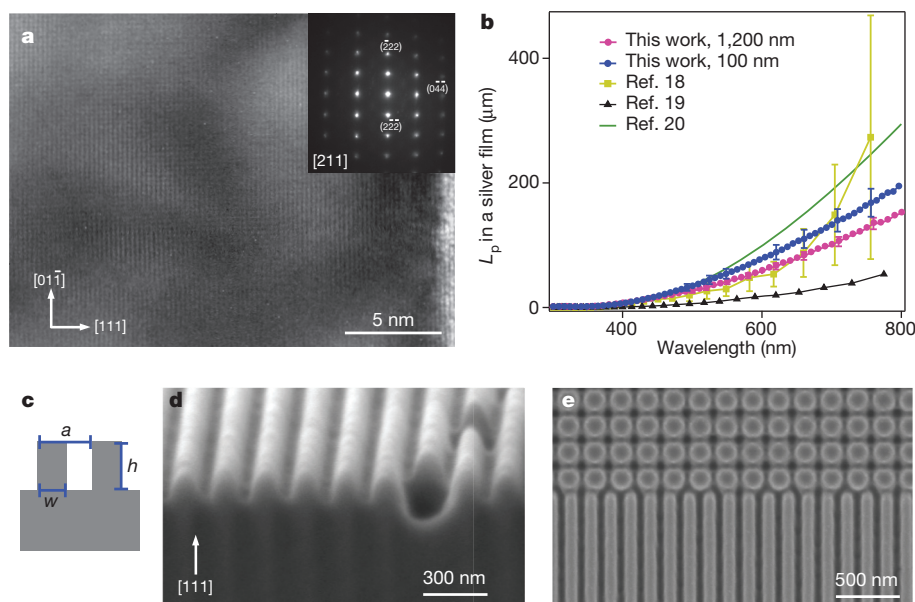
Figure 1 | Single-crystalline silver film and fabricated devices. a, High-resolution transmission electron microscopy image taken down the [211] axis that demonstrates the single-crystalline nature of the sputter-deposited silver. The growth direction is from left to right along the [111] direction with the surface of the silver film shown at the far right of the image. The inset shows the electron diffraction pattern. **b**, SPP propagation length L_p on a silver film derived from measured real and imaginary parts of the dielectric constants for 100-nm-thick (blue circles) and 1,200-nm-thick (pink circles) sputtered films. For comparison, propagation lengths calculated using the dielectric constants reported in refs 18–20 (green line) are also shown (error bars are one standard deviation from the average value). **c**, Schematic of HMS, with pitch a, width w and height h. **d**, A cross-sectional SEM image of a fabricated device. **e**, Top-down SEM image of a silver/air grating and out-coupling structures (top).

Figure 3 illustrates a second device, D2, with $\lambda_T = 560$ nm, which exhibits another remarkable phenomenon: diffraction-free propagation. At λ_T, the flat dispersion curve implies that all SPPs propagate parallel to the silver ridges[11] (Fig. 4b, Supplementary Fig. 12 and discussions below) and thus SPPs excited on a single silver ridge remain primarily confined to the same ridge despite its sub-wavelength width ($\sim\lambda/6$). In device D2, slots defined directly on individual silver ridges serve as in-coupling structures that convert far-field light to SPPs (or out-coupling structures that convert SPPs to far-field light); see Fig. 3a–c. As shown in Fig. 3d, at $\lambda = 585$ nm, despite being excited by only one in-coupling structure, SPPs scatter off multiple out-coupling structures owing to normal, diffractive propagation. However, at $\lambda_T = 560$ nm SPPs primarily scatter off the out-coupling

structure located on the same ridge as the in-coupling structure (Fig. 3e), signifying diffraction-free propagation. This diffraction-free propagation, coupled with suitably designed 'magnifying' out-coupling structures, enables sub-diffraction-resolution imaging and photon routing[6,7]. Figure 3g presents one such demonstration: at $\lambda_T = 560$ nm, despite SPPs being launched at two in-coupling structures separated by a sub-wavelength spacing of 150 nm, SPPs primarily scatter off the two corresponding out-coupling structures staggered along the propagation axis.

We next demonstrate a new optical phenomenon supported by the silver/air grating: the dispersion-dependent plasmonic spin-Hall effect (PSHE)[12,13,23,24], a plasmonic analogue of the electronic Rashba[25] and photonic spin-Hall effects[15,26]. In electronic systems, spin-orbit

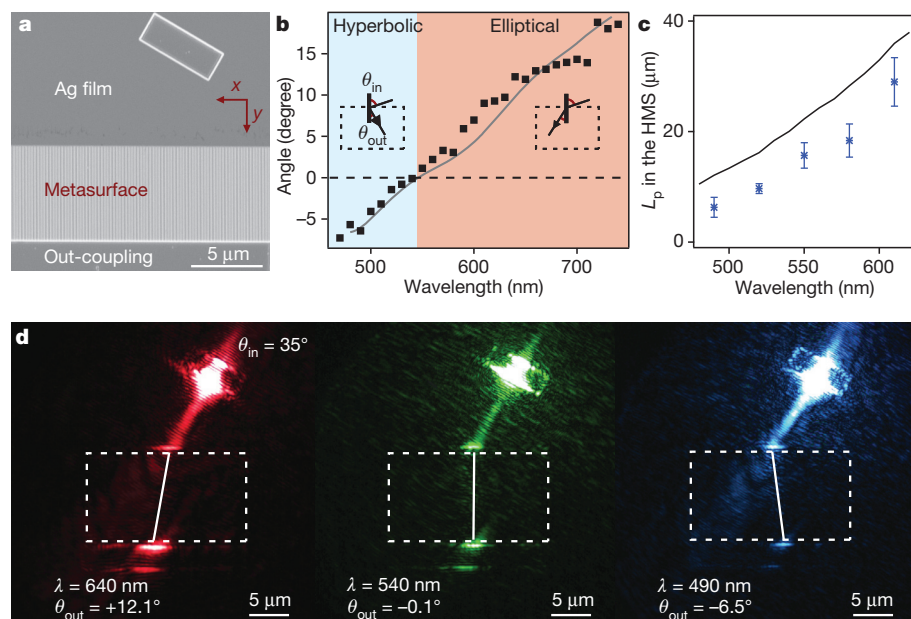**Figure 2 | Measurement of SPP refraction at a flat silver/HMS interface. a**, An SEM image of a device, D1. Far-field light is converted to SPPs in the silver film via the angled rectangular in-coupling structure at the top of the image. The excitation laser is unpolarized. The SPPs propagate along the silver film, are refracted at the film–metasurface interface, and are then scattered into the far field at the out-coupling structure at the bottom of the image. In this device, the height of the silver ridge is 80 nm, the width is 90 nm, and the pitch is 150 nm. **b**, The angle of refraction θ_{out} as a function of wavelength, with elliptical (red-shaded) and hyperbolic (blue-shaded) dispersion regimes indicated. The solid line is the simulated angle of refraction from FDTD simulations. The input and output angles, θ_{in} and θ_{out}, are defined in the inset, with the dotted box indicating the region of the HMS. **c**, The experimentally measured (blue data points) and simulated (black line) propagation length L_p of SPPs in the HMS (error bars are one standard deviation from the average value). **d**, Images of SPP refraction at the flat silver/HMS interface. The dashed boxes indicate the region of the HMS.
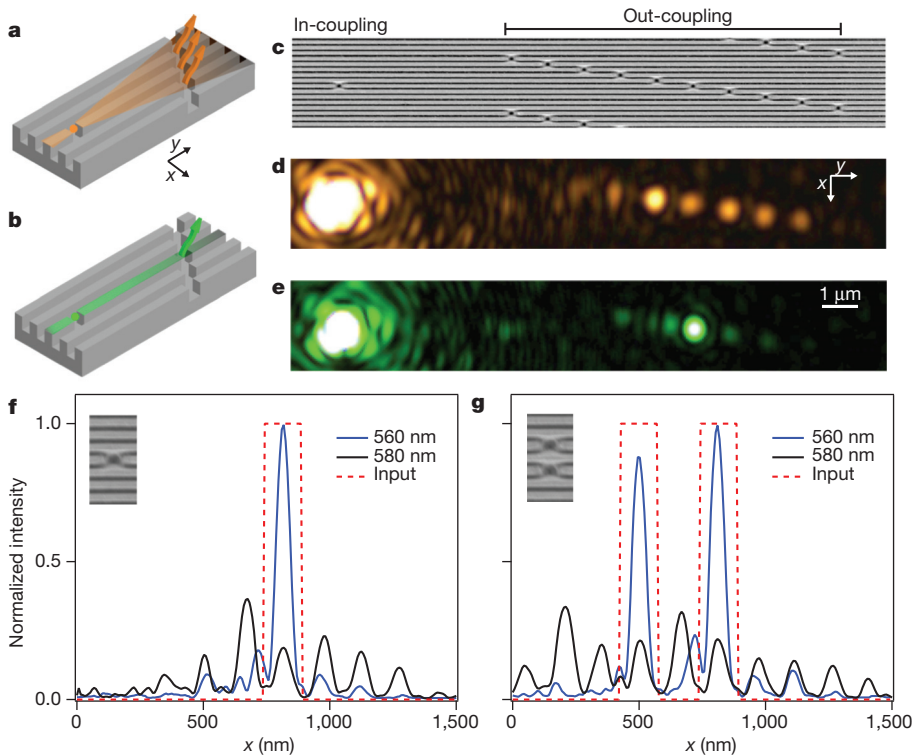
Figure 3 | Observation of diffraction-free SPP propagation. a, A schematic for SPP diffraction in a silver/air grating. **b**, A schematic for diffraction-free SPP propagation in a silver/air grating. In **a** and **b** an in-coupling structure defined on a single ridge (left-hand side) acts as a point source of SPPs. SPPs scatter off at the out-coupling structures on the other side that are staggered along the y axis for magnification. **c**, An SEM image of a device, D2. The height of the silver ridge is 80 nm, the width is 90 nm, and the pitch is 150 nm. The y-axis distance between out-coupling structures is 1 μm, thus providing the magnification of 6.7. **d**, **e**, Optical images of SPPs scattering at the out-coupling slots (right-hand side) with SPPs excited with unpolarized light by a single in-coupling structure (inset to Fig. 3f) for $\lambda = 585$ nm (**d**) and $\lambda = \lambda_T = 560$ nm (**e**). **f**, Diagonal cross-sections of optical image across out-coupling slots at $\lambda = 560$ nm (blue) and $\lambda = 585$ nm (black), with the input position marked in red. The x-axis coordinate of the cross-section is indicated on the bottom axis. **g**, Similar cross-sections obtained when two in-coupling notches (inset) are used. In **f** and **g**, the out-coupling intensities are normalized such that the total integrated intensities are equal.

coupling arises due to the lack of inversion symmetry (for example, in the presence of an external electric field) and couples the spin of a charge carrier to its propagation direction. Similarly, in an optical system with tightly confined optical modes, the light propagation direction couples to the electric field rotation, leading to the photonic spin-Hall effect[15,26]. In the HMS, a PSHE arises from three structural features of the silver/air grating. First, this structure lacks inversion symmetry and exhibits high optical anisotropy for SPPs propagating

parallel and perpendicular to the silver ridges (y- and x-axes, respectively, in Fig. 4a). Second, due to its nanoscale ridged structure, the HMS can support electric field components perpendicular to the SPP propagation direction (for example, E_z and E_x for propagation along y), and thus SPPs can exhibit circular polarization. Third, the dispersion of the system is strongly frequency dependent, such that the direction of the SPP group velocity changes when moving from hyperbolic to elliptical polarization. Combined together, these three features enable
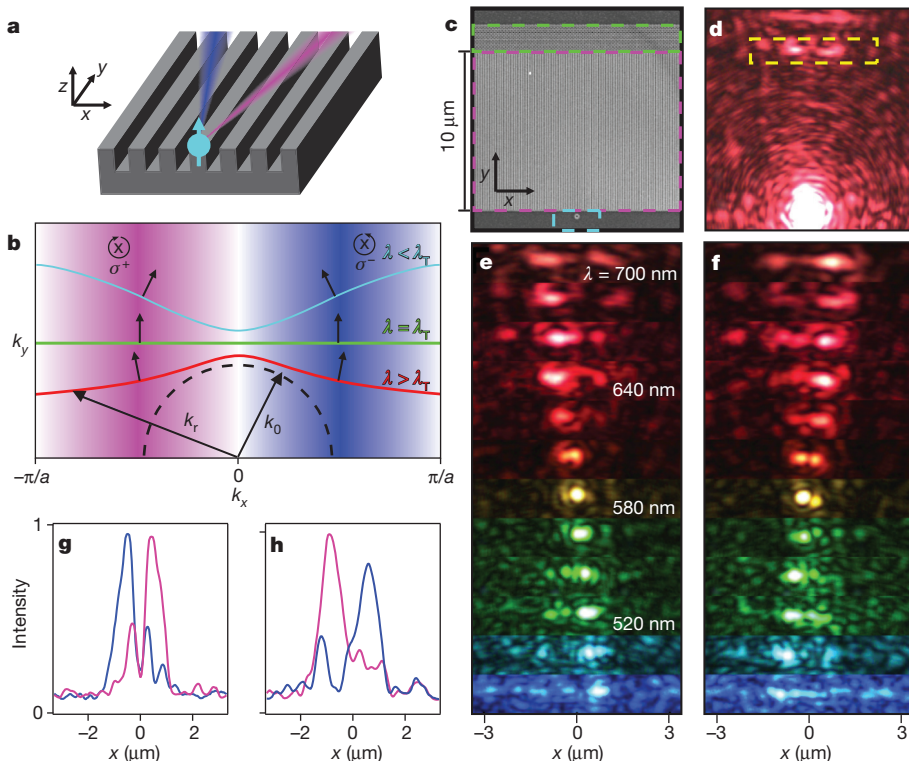

Figure 4 | The dispersion-dependent plasmonic spin-Hall effect (PSHE). a, A schematic of the PSHE. In a silver/air grating, SPPs with different helicities propagate into distinct spatial directions. **b**, Illustration of the origin of the PSHE. Positive k_x corresponds to σ^- (blue shading) and negative k_x to σ^+ (magenta shading). The direction of the group velocity (black arrows) is perpendicular to the isofrequency contours at a given dispersion regime: elliptic (red), diffractionless (green), and hyperbolic (cyan). The allowed k_x values extend from $-\pi/a$ to $+\pi/a$, where a is the pitch of the silver/air grating. The dotted black line indicates the free-space isofrequency contour at the same frequency as the red curve. **c**, An SEM image of a device, D3, used to examine PSHE with an in-coupling structure (cyan rectangle), a silver/air grating (pink rectangle), and out-coupling cylinders (green rectangle). **d**, Image of D3 under unpolarized laser excitation of the in-coupling structure. The out-coupling region is marked by the yellow box. **e**, **f**, Image from the out-coupling structures as a function of wavelength collecting only σ^+ (**e**) and σ^- (**f**) polarized light. From bottom to top, the wavelength increases from 480 nm to 700 nm in increments of 20 nm. **g**, **h**, Light intensities measured at the out-coupling structures for σ^+- (magenta) and σ^-- (blue) polarized light at $\lambda = 530$ nm (**g**) and $\lambda = 640$ nm (**h**).

the dispersion-dependent PSHE in which the SPP propagation direction and helicity are linked to each other in a frequency-dependent manner (Fig. 4). While the PSHE has been experimentally observed in bulk hyperbolic metamaterials at radio frequencies[14], it has not previously been realized experimentally in the visible frequency regime.

Figure 4c shows a device, D3, which demonstrates the PSHE. In this device, a single circular in-coupling structure near the silver/air grating scatters unpolarized far-field light to propagating SPP modes, and an array of vertical silver cylinders on the other side (diameter 140 nm, height 90 nm) comprises an out-coupling structure that scatters SPPs back to the far field. These out-coupling structures convert the SPP polarization into far-field polarization with minimal distortion (see discussions in Supplementary Fig. 13). As shown in Fig. 4d, when SPPs are excited by the in-coupling structure, they split into two separate (left- and rightward) beams. Polarization-resolved imaging reveals that these split SPP beams exhibit opposite circular polarizations (one predominantly ($\sim$80%) σ^+ and the other is σ^- with $\sigma^\pm = E_x \pm iE_z$; Fig. 4g and h). Moreover, this helicity-dependent splitting is strongly wavelength-dependent (Fig. 4e and f). When the silver/air grating exhibits an elliptical dispersion ($\lambda > 580$ nm), the σ^+ (σ^-)-polarized SPPs deflect to the left (right), with the deflection angle decreasing with decreasing λ. When the silver/air grating enters the hyperbolic regime ($\lambda < 580$ nm), this behaviour reverses (similar to the magnetic field switching sign in the electronic Rashba effect), and the σ^+ (σ^-)-polarized SPPs deflect to the right (left). At the diffraction-free propagation point ($\lambda_T = 580$ nm), the splitting between σ^+ and σ^- helicities vanishes.

The physical origin of this dispersion-dependent PSHE can be understood using the isofrequency contour schematically illustrated in Fig. 4b. In the silver/air grating, the SPP helicities are determined by the wave vector that characterizes the electric field. The electric field of an SPP mode is given by $E \approx E_r \hat{r} - (k_r/k_z)E_r \hat{z}$, where $k_z = i\sqrt{k_r^2 - k_0^2}$, $k_r = \sqrt{k_x^2 + k_y^2}$ is the plasmonic wavenumber in the direction of $\hat{r}$, $\hat{r}$ is the in-plane direction of k, and k_0 is the free-space wave number given by ω/c, where c is the speed of light in a vacuum[14,27]. Because the SPPs are evanescent perpendicular to the surface, k_z is imaginary and the field rotates along $\hat{r}$. Near the centre of the Brillouin zone ($k_x = 0$), we have $k_r \approx k_y \approx k_0$, and the SPP wavelength λ_{SPP} in our structures is similar to the far-field wavelength λ (Supplementary Fig. 14 and see discussion below). As k_x increases, however, k_r continuously increases due to highly anisotropic dispersion relation, and for $k_r \gg k_0$ the modes become circularly polarized in the x–z plane. Near the edge of the Brillouin zone, modes of opposite circular polarization hybridize, and the polarization effects in the x–z plane vanish. These considerations indicate that when projected on the x–z plane, an SPP mode with $k_x < 0$ ($k_x > 0$) exhibits σ^+ (σ^-) polarization (note that an SPP with $k_x = 0$ will exhibit electric field rotation in the y–z plane[15]). The direction of SPP propagation is, however, governed by the group velocity vector that is perpendicular to the isofrequency contour. The small angular spread of the right- and leftward SPP beams is a consequence of the shape of this isofrequency contour, which reflects the optical anisotropy of our silver/air grating. As shown in Fig. 4b, this simple consideration explains our experimental observations. Specifically, when the device exhibits elliptical dispersion ($\lambda > \lambda_T$), the σ^+ (σ^-)-polarized SPPs deflect to the left (right) because the leftward (rightward) group velocity vector is associated with $k_x < 0$ ($k_x > 0$). In contrast, in the hyperbolic dispersion regime ($\lambda < \lambda_T$), the reverse is true, leading to the switching of the deflection directions for σ^+ (σ^-)-polarized SPPs.

A key improvement of our approach is the dramatic reduction in optical losses in comparison to bulk metamaterials. To directly characterize the optical performance of HMS, we fabricated silver/air gratings of varying lengths with identical light in- and out-coupling structures, and measured the out-coupled light intensity as a function of the grating length at the same in-coupling intensity. By fitting the intensity-length curve by a single exponential at a given λ, we then

determined L_p in our devices, ranging from 6 μm at $\lambda = 490$ nm up to 29 μm at $\lambda = 610$ nm (blue stars in Fig. 2c; for discussion see Supplementary Fig. 15). These propagation length L_p values are one to two orders of magnitude larger than those reported in bulk visible-frequency hyperbolic metamaterials[3,4].

To analyse our observations quantitatively, we carried out detailed finite-difference time-domain (FDTD) simulations of SPP propagation in our device geometries (D1 through D3). These FDTD simulations are in good agreement with the experimental observations in Figs 2–4: negative refraction for $\lambda < \lambda_T$ (Fig. 2b, solid line), diffraction-free propagation at λ_T (Supplementary Fig. 12), and the dispersion-dependent PSHE (Supplementary Fig. 16). The FDTD simulations also indicate that the local polarization of the SPP field reaches 87% for left- and right-propagating circularly polarized SPPs, larger than experimentally observed values of 80%, due to the imperfect polarization conversion of our out-coupling structure (Supplementary Fig. 17). The simulated propagation lengths (black line in Fig. 2c; for discussion see Supplementary Information) in the HMS are $\sim$30% larger than the experimentally determined ones, probably owing to residual nanoscale roughness introduced during the fabrication procedure. Owing to increasing SPP confinement, the sensitivity to surface roughness increases at lower wavelengths, resulting in greater scattering losses. Despite these imperfections, the measured propagation distances indicate that the low-loss, two-dimensional nature of our devices offers a substantial improvement over conventional bulk metamaterials in terms of optical loss, thereby opening the door for a wide array of high-performance plasmonic nanostructures.

Although our demonstrations focused on one particular family of metasurfaces, that is, a silver/air grating, the fabrication strategy is general and compatible with other bottom-up and top-down semiconductor and metal processing techniques. Our method thus opens up the possibility of realizing low-dimensional transformation optics and metamaterial-based devices[28,29]. The same method can be used to generate integrated metamaterial circuits that combine HMSs on-chip with other optoelectronic and plasmonic devices. The HMSs can enable quantum optics applications as well. Because of their small mode volumes and increased plasmonic density of states[10,11], HMSs can be used for enhancing interactions of SPPs with individual quantum emitters—a new pathway for realizing solid-state quantum nonlinear optical circuits. Moreover, the frequency-dependent spin–orbit interaction enables the exploration of a new class of solid-state quantum optical phenomena that involve chiral optical interfaces with quantum emitters. By extending recent demonstrations involving such interactions with one-dimensional waveguides[15] into two dimensions, this could enable spin-dependent routeing of single photons as well as non-trivial topological phenomena that combine spin–orbit interactions with single photon nonlinearities associated with quantum emitters[30].

1. Pendry, J. B. Negative refraction makes a perfect lens. *Phys. Rev. Lett.* **85**, 3966–3969 (2000).
2. Shelby, R. A., Smith, D. R. & Schultz, S. Experimental verification of a negative index of refraction. *Science* **292**, 77–79 (2001).
3. Yao, J. *et al.* Optical negative refraction in bulk metamaterials of nanowires. *Science* **321**, 930 (2008).
4. Naik, G. V. *et al.* Epitaxial superlattices with titanium nitride as a plasmonic component for optical hyperbolic metamaterials. *Proc. Natl Acad. Sci. USA* **111**, 7546–7551 (2014).
5. Esfandyarpour, M., Garnett, E. C., Cui, Y., McGehee, M. D. & Brongersma, M. L. Metamaterial mirrors in optoelectronic devices. *Nature Nanotechnol.* **9**, 542–547 (2014).
6. Salandrino, A. & Engheta, N. Far-field subdiffraction optical microscopy using metamaterial crystals: theory and simulations. *Phys. Rev. B* **74**, 075103 (2006).
7. Liu, Z. W., Lee, H., Xiong, Y., Sun, C. & Zhang, X. Far-field optical hyperlens magnifying sub-diffraction-limited objects. *Science* **315**, 1686 (2007).
8. Shalaev, V. M. Optical negative-index metamaterials. *Nature Photon.* **1**, 41–48 (2007).
9. Poddubny, A., Iorsh, I., Belov, P. & Kivshar, Y. Hyperbolic metamaterials. *Nature Photon.* **7**, 948–957 (2013).

10. Kildishev, A. V., Boltasseva, A. & Shalaev, V. M. Planar photonics with metasurfaces. *Science* **339**, 1232009 (2013).
11. Liu, Y. M. & Zhang, X. Metasurfaces for manipulating surface plasmons. *Appl. Phys. Lett.* **103**, 141101 (2013).
12. Lin, J. *et al.* Polarization-controlled tunable directional coupling of surface plasmon polaritons. *Science* **340**, 331–334 (2013).
13. Rodriguez-Fortuno, F. J. *et al.* Near-field interference for the unidirectional excitation of electromagnetic guided modes. *Science* **340**, 328–330 (2013).
14. Kapitanova, P. V. *et al.* Photonic spin Hall effect in hyperbolic metamaterials for polarization-controlled routing of subwavelength modes. *Nature Commun.* **5**, 3226 (2014).
15. Petersen, J., Volz, J. & Rauschenbeutel, A. Chiral nanophotonic waveguide interface based on spin-orbit interaction of light. *Science* **346**, 67–71 (2014).
16. Baski, A. A. & Fuchs, H. Epitaxial growth of silver on mica as studied by AFM and STM. *Surf. Sci.* **313**, 275–288 (1994).
17. Park, J. H. *et al.* Single-crystalline silver films for plasmonics. *Adv. Mater.* **24**, 3988–3992 (2012).
18. Johnson, P. B. & Christy, R. W. Optical constants of noble metals. *Phys. Rev. B* **6**, 4370–4379 (1972).
19. Palik, E. D. *Handbook of Optical Constants of Solids* Vol. 3 353–357 (Academic Press, 1998).
20. Wu, Y. *et al.* Intrinsic optical properties and enhanced plasmonic response of epitaxial silver. *Adv. Mater.* **26**, 6106–6110 (2014).
21. Fan, X. B., Wang, G. P., Lee, J. C. W. & Chan, C. T. All-angle broadband negative refraction of metal waveguide arrays in the visible range: theoretical analysis and numerical demonstration. *Phys. Rev. Lett.* **97**, 073901 (2006).
22. Smith, D. R. & Schurig, D. Electromagnetic wave propagation in media with inde finite permittivity and permeability tensors. *Phys. Rev. Lett.* **90**, 077405 (2003).
23. Lee, S. Y. *et al.* Role of magnetic induction currents in nanoslit excitation of surface plasmon polaritons. *Phys. Rev. Lett.* **108**, 213907 (2012).
24. Huang, L. L. *et al.* Helicity dependent directional surface plasmon polariton excitation using a metasurface with interfacial phase discontinuity. *Light Sci. Appl.* **2**, e70 (2013).
25. Bychkov, Y. A. & Rashba, E. I. Oscillatory effects and the magnetic susceptibility of carriers in inversion layers. *J. Phys. C* **17**, 6039–6045 (1984).
26. Onoda, M., Murakami, S. & Nagaosa, N. Hall effect of light. *Phys. Rev. Lett.* **93**, 083901 (2004).
27. Raether, H. *Surface Plasmons on Smooth and Rough Surfaces and on Gratings* Ch. 1 (Springer, 1988).
28. Silva, A. *et al.* Performing mathematical operations with metamaterials. *Science* **343**, 160–163 (2014).
29. Huang, K. C. Y. *et al.* Electrically driven subwavelength optical nanocircuits. *Nature Photon.* **8**, 244–249 (2014).
30. Hafezi, M., Demler, E. A., Lukin, M. D. & Taylor, J. M. Robust optical delay lines with topological protection. *Nature Phys.* **7**, 907–912 (2011).

Author Contributions A.A.H. and H.P. conceived the study, and A.A.H., R.C.D., M.D.L. and H.P. designed the experiments. A.A.H., R.C.D., A.D. and N.P.d.L. developed the fabrication procedure. A.A.H., R.C.D., A.D. and M.P. performed experiments. A.A.H., R.C.D., D.S.W. and J.P. performed computational analyses and simulations. A.A.H., R.C.D., D.S.W., J.P., N.P.d.L., M.D.L. and H.P. contributed to theoretical descriptions. A.A.H., R.C.D., D.S.W., J.P., M.D.L. and H.P. wrote the manuscript, with extensive input from all authors.

Author Information Reprints and permissions information is available at www.nature.com/reprints. The authors declare no competing financial interests. Readers are welcome to comment on the online version of the paper. Correspondence and requests for materials should be addressed to H.P. (hongkun_park@harvard.edu) and M.D.L. (lukin@physics.harvard.edu).